D.B. Proud, M.J. Evans, Q.N. Chan, P.R. Medwell

Characteristics of turbulent flames in a confined and pressurised jet-in-hot-coflow combustor

Journal of the Energy Institute, 2022; 105:103-113

Published at: http://dx.doi.org/10.1016/j.joei.2022.07.007

Characteristics of turbulent flames in a confined and pressurised jet-in-hot-coflow combustor

D.B. Proud[a], M.J. Evans[a,b], Q.N. Chan[c], P.R. Medwell[a]

[a] *School of Mechanical Engineering, The University of Adelaide, Adelaide, SA 5005, Australia*
[b] *UniSA STEM, University of South Australia, Mawson Lakes, SA 5095, Australia*
[c] *School of Mechanical and Manufacturing Engineering, University of New South Wales, Sydney, NSW 2052, Australia*

Abstract

Combustion in hot and low oxygen environments, such as those encountered in practical devices including inter-turbine burners and sequential gas turbines, is not yet fully understood at a fundamental level, particularly in terms of the effects of pressure. To meet this gap in understanding, a confined-and-pressurised jet-in-hot-coflow (CP-JHC) combustor has been developed to facilitate optical diagnostics of turbulent flames in hot and vitiated coflows for the studies of flame stabilisation, structure and soot formation at elevated pressures. The CP-JHC burner has been designed for steady operation at 10 bar with internal temperatures of up to 1975 K, with a water-cooled central jet issuing into a hot oxidant stream of combustion products from a non-premixed natural gas/H_2 burner. This work describes the key features and operational capabilities of the CP-JHC burner and presents a selection of experimental results showing characteristics not previously available. Specifically, temperature measurements of the hot coflow are used to estimate the enthalpy deficit of the stream, revealing an increase in thermal efficiency with increasing heat input, and a decrease with increasing pressure. Chemiluminescence imaging of OH* and CH* is performed for turbulent jet flames to study the flame structure under various operating conditions, and true-colour imaging results are also included to highlight the change in soot formation under elevated pressures. The mean images indicate a change in stabilisation behaviour with changes in pressure and jet Reynolds number (Re_{jet}), which is further investigated by a statistical analysis of the short-exposure CH* images. This analysis reveals that an increase in Re_{jet} from 10,000 to 15,000 leads to an increase in the mean lift-off height (from the jet exit plane) from approximately 1.5 to 6 jet diameters at atmospheric pressure, while the flames at elevated pressures show significantly less variation and tend to stabilise at the jet exit for $P > 3.5$ bar(a). The experimental findings are complemented by numerical simulations of laminar opposed flow flames, providing additional insights into the fundamental chemical kinetics effects which

*Corresponding author. E-mail: douglas.proud@adelaide.edu.au

influence these flames. In particular, a monotonic reduction in both the maximum and integrated OH^* and CH^* mass fractions is observed with increasing pressure. This reduction is particularly pronounced at lower pressures, with a reduction to 10% of the atmospheric-pressure value at 3 bar(a) for the integrated OH^* mass fraction. Additionally, this behaviour is shown to be related to the combined effects of a shift in the formation pathways and the increased impact of collisional quenching.

Keywords: Elevated pressure combustion, Mild combustion, Turbulent flames, Jet-in-hot-coflow, Chemiluminescence

---

1. Introduction

The reduction of pollutant emissions, in conjunction with improvements in efficiency and operational flexibility, are major challenges in the development of new combustion devices. A promising technology in this regard is "mild" combustion, which, in addition to describing the nature of the combustion process, is an acronym for moderate or intense low-oxygen dilution combustion. This mode of combustion, which is also referred to as flameless combustion and flameless oxidation [1, 2], is characterised by a highly diluted oxidant stream which is above the auto-ignition temperature of the fuel [3]. In practice, such conditions are typically achieved via exhaust gas recirculation (EGR) or the use of a secondary combustion stage. The use of exhaust gas heat allows an increase in the thermal efficiency, while the low oxygen concentration results in lower peak temperatures, thus limiting the production of NO_x, a major pollutant associated with combustion. Another important feature of mild combustion is the reduced tendency for soot formation in this regime, which is attributed to a shift in the heat release profile such that pyrolytic regions of negative heat release are suppressed [4].

A potential application of mild combustion is in gas turbines, for both electricity generation and aerospace propulsion applications [1]. The most common approach for practical implementations of mild combustion is via the EGR method, using either internal recirculation (e.g. with a high-momentum jet to generate recirculation zones) or the external recirculation of flue gases. Another potential option which is particularly relevant for gas turbines is the use of a sequential combustion configuration, in which the exhaust products of a primary or initial combustor pass through to a downstream combustion zone into which a secondary fuel stream is injected. Such a configuration—which is referred to as either a sequential gas turbine (SGT) or inter-turbine burner (ITB) depending on the geometry [5, 6, 7, 8, 9]—may be beneficial as it can provide additional fuel-flexibility while avoiding the issue of pressure loss, an inherent challenge of EGR-based gas turbines [1]. There are, however, a number of complexities involved in the implementation of mild combustion in a gas turbine, largely due to the requirement of a variable output and the need to operate at a range of pressures and temperatures. While mild combustion is relatively

well understood for the case of atmospheric pressure (such as in a furnace), the impact of increased pressure on the formation of emissions and stability of the mild regime requires further investigation [10], to enable the extension of its application to devices such as gas turbines.

Due to the relevance of the topic to practical applications, the effect of pressure on combustion has remained an active area of investigation for some time. An inherent challenge associated with experiments at elevated pressure is the difficulty in obtaining data relating to flame structure and stabilisation, since the need for confinement tends to limit optical access for diagnostics. A useful technique in this regard is chemiluminescence imaging, which facilitates the investigation of flame structure and reaction zone features through a single viewing window. This imaging is typically focussed on the excited-state OH and CH species (termed OH^* and CH^*), as they tend to be correlated with regions of high heat release and radical concentrations [11]. One of the challenges associated with chemiluminescence imaging is the difficulty in extracting quantitative information (such as heat release rate) from the measurements, since several factors—including pressure—can influence the excitation and subsequent relaxation of the species [12, 13]. Recently, laser diagnostic measurements have been performed for turbulent flames at pressures up to 12 bar for turbulent non-premixed flames with a $CO/H_2/N_2$ fuel mixture issuing into a coflow of air [14]. Imaging of the near-field reaction zone revealed both a narrowing of the OH layer and a reduced probability of local extinction with increasing pressure [14]. The formation of soot is also known to be particularly sensitive to pressure, with previous studies suggesting a linear relationship between soot volume fraction and operating pressure [15], as well as a shift in the onset of the sooting region further upstream for elevated pressures, even when velocity is held constant [16]. Although mild conditions are known to suppress soot formation, this is primarily based on observations at atmospheric pressures; it is therefore imperative to explore the competing effects of pressure and dilution by exhaust products on the formation of soot.

There have also been a number of important studies based on conditions relevant to mild and sequential combustion at elevated pressures. A particular configuration that has been studied in-depth is the FLOX® combustor [17, 18], which is based on a high-momentum, recirculation concept. Optically accessible experiments with the FLOX® combustor highlighted the importance of the jet exit conditions on the mixing processes and the resulting emissions characteristics, with OH^* chemiluminescence and OH-PLIF reaction-zone imaging confirming the existence of distributed reaction zones (typical of mild combustion) in the low-emissions operating range [17]. Turbulent jets issuing into a hot cross-flow of combustion products under pressurised conditions have also been investigated, with high-speed imaging revealing that the flame stabilisation process is particularly sensitive to the addition of natural gas to hydrogen, as well as highlighting the importance of isolated ignition kernels on the overall autoignition process [19]. The ignition and stabilisation features of flames in conditions relevant to sequential gas turbines have also been studied, with a numerical analysis involving both 1-D simulations and LES modelling by Schulz

and Noiray [20] identifying a range of possible combustion modes which can co-exist in such a configuration. Additionally, Guethe et al. [21] provide a comprehensive overview of the potential of chemiluminescence to aid in the development, control and optimisation of gas turbines, including as a diagnostic tool to further understand the flame dynamics in sequential combustors. While these studies provide valuable insights into the behaviour of flames under hot and low-oxygen conditions at pressure, they tend to feature relatively complex geometries which—although beneficial in terms of demonstrating the viability of the technology—leads to coupling between boundary conditions and limits the applicability of the results for model validation [10].

In contrast to the aformentioned studies at elevated pressures, there have been several studies performed in open-flame burners at atmospheric pressure which facilitate the decoupling of chemistry, mixing and flow-field effects. Many of these experiments have been carried out using so-called jet-in-hot-coflow (JHC) burners [22, 23], or similar designs such as the vitiated coflow burner [24, 25]. In these burners, mild combustion conditions are achieved using an additional burner upstream of the main combustion zone, with the primary fuel jet issuing into the hot and low-O_2 coflow of combustion products. This configuration emulates EGR conditions, or the secondary stage of an SGT or ITB. The advantage of the JHC and similar designs is the fact that the upstream combustion zone can be controlled independently of the jet, allowing the coflow properties, such as O_2 concentration and temperature, to be varied while maintaining constant jet boundary conditions, such as Reynolds number and fuel type.

To enhance the fundamental understanding of mild combustion in conditions relevant to devices such as gas turbines, the current investigation is focussed on the structure, stability and sooting behaviour of turbulent flames at elevated pressures, in a hot and low-O_2 coflow. Experiments have been performed using a unique burner which combines the advantages of the well-studied JHC configuration with the ability to operate at pressure. The design and operation of this "confined and pressurised jet-in-hot-coflow" combustor (CP-JHC) is described in this paper, along with a series of experimental results. This includes a characterisation of the coflow, in terms of the effect of pressure, equivalence ratio and heat input on the downstream temperature of the coflow stream. Chemiluminescence and true-colour imaging is performed to examine the effect of pressure on the characteristics of jet flames with Reynolds numbers of 10,000 and 15,000 issuing into a 9% O_2 coflow. These results are supplemented by laminar flame simulations, which facilitate the detailed analysis of the change in chemical kinetics with increasing pressure, and its implications regarding chemiluminescence intensity. This is of particular importance to guide future research efforts in developing the ability to extract quantitative information from chemiluminescence imaging, which will in turn aid in the development and validation of CFD models.

2. Methods

2.1. Burner description

A cross-sectional schematic which highlights the key features of the CP-JHC combustor is shown in Fig. 1. The jet flame and hot coflow are contained within a 100-mm-diameter cylindrical quartz tube, which is surrounded by a section of DN300 (O.D. of 324 mm), 304 stainless steel seamless pipe with a wall thickness of 12.7 mm. The void between the quartz and the pipe wall is filled with thermal insulation to allow steady operation at 10 bar with internal temperatures up to 1975 K without a requirement for cooling the main pressure vessel walls. This configuration minimises heat losses in the system, allowing for the investigation of hotter coflow conditions and with minimal thermal boundary layer. The hot combustion products from the jet and coflow are then cooled via water jackets, allowing the pressure in the vessel to be controlled via a back-pressure regulator (cooling/exhaust system is not shown in Fig. 1).

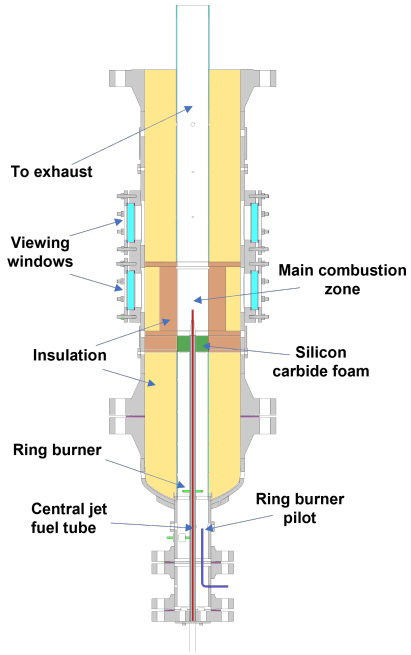

Figure 1: CP-JHC cross section with main components labelled. Note: the exhaust section of the combustor has been omitted from this figure.

The hot and low-O_2 coflow is produced using a ring burner, via the non-premixed combustion of a natural gas (NG) and H_2 fuel mixture with an air stream which enters upstream of the ring burner. The ring burner is initially ignited with a pilot flame, which is then extinguished following stabilisation. The flowrates of NG, H_2 and air can be independently varied to provide a range

of coflow conditions, with the option of diluting the air stream with N_2 to obtain specific O_2 concentrations and temperatures with constant coflow velocity [22, 23]. The main fuel stream issues into the coflow of combustion products from a 4.6-mm-diameter jet, which is readily interchangeable to facilitate measurements with other jet diameters. The central jet is water-cooled to avoid structural damage or thermal decomposition of the fuel, and the length of the jet is nearly 300 times its internal diameter to ensure fully-developed flow at the exit plane. The combustor has the capability for 8 windows to be installed at two different heights (as shown in Fig. 1), although the current configuration features a single quartz window (48 mm×107 mm) positioned level with the jet exit plane, with the others blanked-off with thermal insulation. This viewing window facilitates the optical analysis of the jet flames issuing into the hot coflow of combustion products. An annulus composed of porous silicon carbide foam is positioned below the viewing window, upstream of the jet exit plane in order to improve the uniformity of the flow. It is worth noting that the CP-JHC is a research burner developed for the investigation of flame structure and stabilisation in a specific location within the burner; consequently, the emissions characteristics—which are a global feature of the combustor—are not a focus of the experiments.

2.2. Boundary conditions and experimental techniques

Turbulent flames were stabilised in a hot and low-O_2 coflow in the CP-JHC burner. The ring burner fuel is NG blended with H_2 in a 1:1 volumetric ratio to improve stability and reduce formation of soot at increased pressures. Air was used as the oxidant, and the air-fuel ratio and total fuel flowrate were modified to provide a range of coflow O_2 concentrations (X_{O_2}) and heat inputs (Q_{in}), respectively. Coflow temperatures (T_{meas}) were monitored *in-situ* with an R-type thermocouple which was located level with the jet exit plane, halfway between the central axis and the inner wall of the insulation. As mentioned previously, the insulation surrounding the combustor walls minimises the prominence of the thermal boundary layer. Similarly, the water-cooled jet is covered with an alumina sheath to minimise heat transfer. With these features, the impacts of a thermal boundary layer are ameliorated. Additionally, the temperature across the core of the coflow is homogenised by the silicon carbide foam which is positioned upstream of the jet exit. Ultimately, the spatial variations in the coflow temperature are at most 10%, and the effect of these variations is reflected in the experimental uncertainty that is reported throughout the paper. Presented temperature measurements for coflow characterisation were taken without a jet flame to minimise additional incident radiation on the thermocouple. The coflow characterisation results presented in this paper correspond to equivalence ratios (Φ) ranging from 0.3–0.85 (excess O_2 of 3 to 14% vol.), with heat inputs ranging from approximately 4–22 kW; these two variables in turn correspond to variations in the temperature, O_2 concentration and velocity ($\bar{U}$) of the coflow.

Turbulent jet flames with a 1:1 (by volume) blend of NG ($\geq$ 92% CH_4) and H_2 issuing into the hot coflow were also investigated. Two different jet

Table 1: Coflow boundary conditions and equilibrium species concentrations (X) for the NG:H_2 jet flame results.

P [bar(a)]	$\bar{U}$ [m/s]	T_{meas} [K]	T_{ad} [K]	Q_{in} [kW]	X_{O_2} [%]	X_{CO_2} [%]	X_{H_2O} [%]	X_{N_2} [%]
1.1–7	3.6–0.57	1025±25	1595	8.7	9.0	4.3	13	73

Reynolds numbers (Re_{jet}) of 10,000 and 15,000 were used throughout the investigation; these were maintained across the different pressures to examine the effects of pressure and Re_{jet} independently. The chemiluminescence imaging results presented for the turbulent jet flames herein correspond to constant coflow conditions at the various pressures; these are shown in Table 1.

Images of the jet flames were captured using both a DSLR camera and an intensified CCD camera with a UV lens. The DSLR camera was fitted with a 430 nm bandpass filter (FWHM of 10 nm), enabling the imaging of CH^* chemiluminescence. True-colour photographs (i.e. without the filter installed) were also captured with the DSLR camera to study the broadband luminescence. The UV-ICCD camera was also fitted with a bandpass filter, centred at 310 nm with a FWHM of 10 nm to target the chemiluminescence from OH^* radicals. Both cameras were manually focussed, and images were captured with a range of exposure times, f-numbers and ISO-speeds/gains—these settings are reported in this paper where appropriate, and consistency is ensured when directly comparing images from different flame cases. A series of short-exposure CH^* images were also captured with the DSLR camera, facilitating the statistical analysis of the flames in greater detail.

2.3. Numerical simulations

Numerical simulations were performed for 1-D, laminar opposed flow flames under a range of conditions, using the OPPDIF code available in CHEMKIN-PRO. The GRI-Mech 3.0 chemical kinetics mechanism was used to model the combustion of a 1:1 mixture of CH_4 and H_2, with a hot and low-O_2 oxidant stream ($T = 1050$ K, $X_{O_2} = 0.09$) to match the experimental conditions. GRI-Mech 3.0 is a well-established detailed kinetics mechanism available for natural gas combustion under a range of conditions, including pressures up to 20 atm [26]. The rate constant parameters for GRI-Mech are informed by laboratory experiments and theoretical formulations, with the resulting mechanism subjected to a series of sensitivity analyses and parameter optimisations, and the final parameter set then checked against validation datasets available in the literature. This mechanism has been used extensively in the context of CFD modelling, to reproduce the behaviour observed for JHC flames at atmospheric pressure [27, 28, 29], as well as in laminar flame simulations [30]. It is also worth noting that GRI-Mech 3.0 is a more sophisticated version of its predecessors in GRI-Mech 2.11 and GRI-Mech 1.2, which have also been used previously in combustion models involving hot and low-oxygen conditions, including studies based the JHC configuration [31], and similar burners such as the vitiated coflow burner [32, 33]. These mechanisms have also been used to develop reduced mechanisms such as DRM19 and DRM22 [34], as well as in comparisons against

other, less detailed mechanisms such as KEE [35]. These reduced mechanisms—particularly DRM19—have again been used successfully to model combustion under similar hot and low-oxygen conditions [36, 37, 38, 39], further validating the use of GRI-Mech 3.0 in the current study.

The strain rate was held constant for the simulations at different pressures, with a mean normal strain rate of approximately 40 s^{-1}. In order to compare against the experimental observations, additional reactions for OH^* and CH^* formation were included in the kinetics mechanism. The sub-mechanism used for OH^* formation is based on the following two formation reactions, with rate coefficients obtained from Hall & Petersen [40]:

$$H + O + M \longleftrightarrow OH^* + M \tag{R1}$$

$$CH + O_2 \longleftrightarrow OH^* + CO \tag{R2}$$

The CH^* sub-mechanism is based on the following two reactions, with rate coefficients from Elsamra et al. [41]:

$$C_2 + OH \longleftrightarrow CH^* + CO \tag{R3}$$

$$C_2H + O_2 \longleftrightarrow CH^* + CO_2 \tag{R4}$$

Additionally, quenching reactions were included in the model, using the rate coefficients from Tamura et al. [42]. For the OH^* sub-mechanism, an additional reaction was included in order to model the spontaneous emission process, that is:

$$OH^* \longrightarrow OH + h\nu \tag{R5}$$

For this reaction, a spontaneous emission rate of 1.45×10^6 was assumed [43]. It is worth noting that R5 is the mechanism by which light is emitted and therefore corresponds to the experimental chemiluminescence imaging, so its inclusion provides additional insights in comparing the numerical and experimental results.

Although GRI-Mech 3.0 is valid at elevated pressures, the excited-state OH^* and CH^* sub-mechanisms have only been validated at atmospheric pressures. Nevertheless, it is still of interest to investigate how the model behaves as the pressure is increased, particularly in terms of the underlying species which participate in the excitation reactions. Additionally, the simulations enable the modelling of heat release rate (HRR) as a function of pressure. Since OH^* and CH^* chemiluminescence are often used as indicators for regions of intense heat release in a flame [13, 44], it is useful to compare the trends in HRR with pressure—based on the simulations—with the experimental observations relating to chemiluminescence.

3. Results and discussion

3.1. Coflow characterisation and operational limits

To facilitate the precise control of the coflow conditions for the current and future experiments, it is important to characterise the behaviour of the coflow

under a range of operating conditions. To ensure that the coflow exhibited a consistent and predictable behaviour, temperature measurements were performed for a range of equivalence ratios, heat inputs, and operating pressures. In addition to these measurements, qualitative observations via the viewing window were made to assess the stability of the coflow, in addition to monitoring the integrity of the combustor itself in the form of wall-temperature measurements. Fig. 2 maps the measured coflow temperatures at 1 and 5 bar(a) to combinations of coflow heat input (calculated using the lower heating value of the fuel mixture) and equivalence ratio, producing an "operational window" for the coflow burner. This window is limited by: (i) the requirement for a lean, soot-free coflow; (ii) minimum temperature to ensure self-ignition of the jet; and (iii) maximum operating temperature to avoid overheating the pressure vessel.

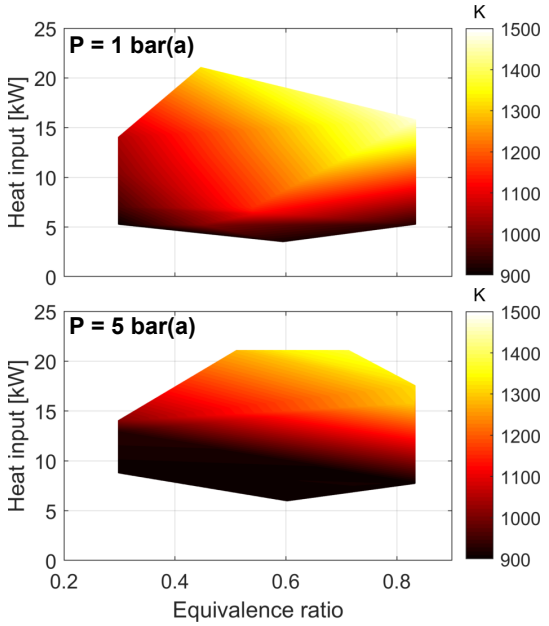

Figure 2: Temperature maps for combinations of coflow heat input and equivalence ratio at 1 and 5 bar(a).

The temperature maps shown in Fig. 2 highlight some interesting results regarding the behaviour of the coflow, particularly when comparing the two different pressures. First of all, both maps show a general increase in the coflow temperature from the bottom-left of the map to the top-right. The increase from left-to-right is expected, since the adiabatic flame temperature increases the closer the equivalence ratio is to unity. The increase in coflow temperature with increasing heat input is due to heat losses to the walls of the combustor, since—despite the insulation surrounding the combustion zone—there is expected to be a departure from the adiabatic flame temperature, emphasising the importance of characterising the coflow. Based on Fig. 2, it appears that

the heat loss is in general greater under the elevated pressure conditions, with a lower coflow temperature for corresponding locations on the map in comparison to the atmospheric case; this is most apparent at low heat inputs and equivalence ratios.

To investigate the heat loss from the coflow under different operating conditions, it useful to quantify this behaviour using the enthalpy deficit (Δh), defined by the following:

$$\Delta h = C_P \times (T_{ad} - T_{meas}) \tag{1}$$

where C_P is the specific heat capacity, T_{ad} is the adiabatic flame temperature, and T_{meas} the measured coflow temperature. Fig. 3 displays the enthalpy deficits calculated using Eq. 1 as a function of operating pressure, from 1–5 bar(a). The values were calculated for three different coflow initial conditions, corresponding to three different heat inputs, all with an adiabatic flame temperature of 1595 K and an equilibrium O_2 concentration of 9% by mole.

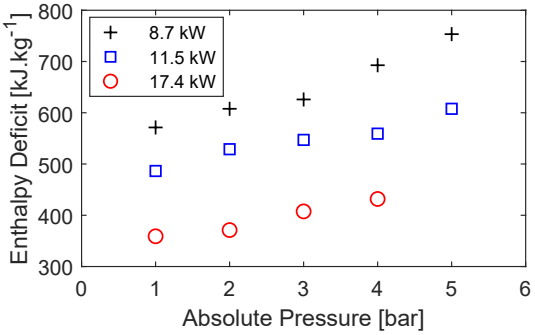

Figure 3: Enthalpy deficits based on measured coflow temperatures, for coflows with three different heat inputs at operating pressures from 1 to 5 bar(a).

The plots shown in Fig. 3 display a clear trend in the enthalpy deficit with both operating pressure and heat input. A consistent decrease in the coflow temperature can be seen with increasing pressure, leading to an approximately linear relationship between enthalpy deficit and operating pressure for all three heat inputs. The increase in heat loss is likely a consequence of the greater residence times as pressure is increased, since the coflow velocity is inversely proportional to operating pressure for coflows of equivalent heat input. This also explains the reduction in enthalpy deficit with increasing heat input, noting that the coflow fuel composition is the same for all three heat inputs, such that the mass flowrate—and therefore the coflow velocity for a given pressure and equivalence ratio—is directly proportional to the heat input. Referring back to Fig. 2, a reduction in equivalence ratio (that is, an increase in the amount of excess air) can actually be seen to lead to an increase in coflow temperature for equivalent heat inputs for certain regions of the map, for example when moving directly right-to-left from $\Phi = 0.8$ to 0.65 with a heat input of approximately

10 kW in the case of the 1 bar map in Fig. 2. This again indicates that the heat losses are related to the coflow velocity, such that the excess air can lead to the heat from the coflow being more effectively transferred downstream despite the reduced flame temperature under certain conditions.

3.2. Mean chemiluminescence imaging

To examine the effect of pressure on the behaviour of turbulent flames issuing into the hot coflow, chemiluminescence imaging of OH^* and CH^* was performed. Fig. 4 displays the results of this imaging for H_2/NG flames with $Re_{jet} = 10,000$ and $Re_{jet} = 15,000$, at operating pressures ranging from 1.1–7 bar(a). The flames shown in Fig. 4 correspond to a coflow of constant heat input and equivalence ratio across the various operating pressures, producing the conditions shown in Table 1. It is worth noting that, although Fig. 3 shows that the operating temperature tends to decrease with increasing pressure if the heat input is held constant, it is possible to exploit the large thermal mass of the system to maintain quasi-constant temperature for the short duration of each individual measurement at different pressures. This is useful as it enables the effect of pressure to be examined for a coflow of constant momentum.

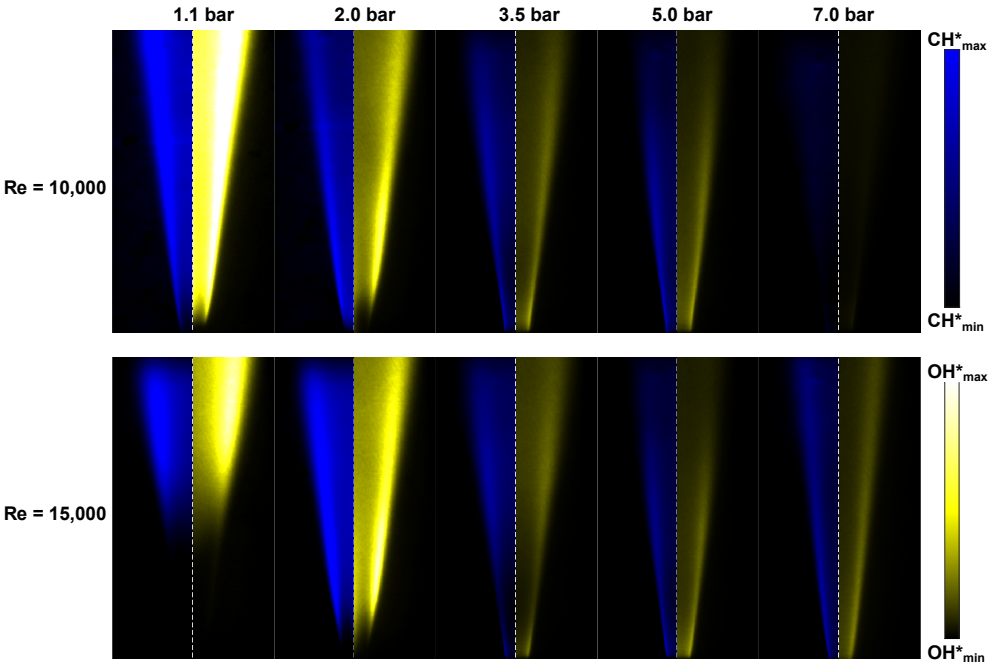

Figure 4: Chemiluminsecnece imaging of 10,000 and 15,000 Reynolds number CH_4/H_2 flames (1:1 blend) at 5 different operating pressures, showing CH^* (left) and OH^* (right). All flames correspond to a 9% O_2 coflow and a nominal coflow temperature of 1025 K ($\pm$25 K). Note: jet exit is located at the bottom of the images, issuing towards the top.

Some interesting changes in flame structure and stability with increasing pressure can be seen from the chemiluminescence imaging results in Fig. 4. For the $Re_{jet} = 10,000$ case at near-atmospheric pressure (i.e. at 1.1 bar), the flame can be seen to be slightly lifted from the jet exit, by approximately half a jet-diameter, based on the OH^* image. It is worth noting that this behaviour is consistent with previous observations based on a flame of equivalent Re_{jet}, fuel mixture and coflow O_2 concentration in an open JHC burner [23]. At 2.0 bar, the flame again appears lifted at first glance; however, upon closer inspection a very faint flame front can be seen to extend to the jet exit. It should be noted that the images shown correspond to long exposure times (20 s in the case of the OH^* images), such that it represents the mean rather than the instantaneous flame structure. The statistical features relating to flame liftoff and stabilisation are presented and analysed in §3.3, in addition to a series of short-exposure OH^* images which are included in Fig. S1 of the Supplementary Material.

The $Re_{jet} = 15,000$ case displays a similar behaviour to the $Re_{jet} = 10,000$ case at 2.0 bar in Fig. 4, although the faint region appears to extend further downstream for the higher Re_{jet} case. At 1.1 bar, the $Re_{jet} = 15,000$ case shows a significant departure, with a less clearly defined flame structure and lift-off location in the near-field which suggests a change in flame stability; this is explored further in §3.3. Interestingly, the 10,000 and 15,000 Re_{jet} flames studied in the open JHC burner both exhibited similar structures, with no noticeable change in stability or lift-off in the near-field [23]. It should be mentioned that the CP-JHC flames presented in Fig. 4 correspond to an approximately 75 K lower coflow temperature to that of the JHC, as well as an increased coflow velocity. These differences—in addition to the absence of entrainment of surrounding air in the confined configuration—are likely responsible for the increased sensitivity to Re_{jet}. For $P > 2.0$ bar, a shift to a flame that is stabilised at the jet exit can be seen for both the 10,000 and 15,000 Re_{jet} cases; this is evident from both the OH^* and CH^* images.

In general, the OH^* and CH^* imaging results both show a similar flame structure for the various cases, with a consistent jet spreading angle of $\approx 7^\circ$ from the jet centreline. It is, however, important to note the change in intensity of the images at different pressures shown in Fig. 4. Specifically, a reduction in intensity with increasing pressure is apparent for both the OH^* and CH^* imaging results in Fig. 4, with a particularly noticeable shift from 2.0 to 3.5 bar for both Reynolds numbers. This is also evident for the $Re_{jet} = 10,000$, 7 bar case, which displays very faint CH^* and OH^* signals which are difficult to distinguish from the background. Interestingly, the $Re_{jet} = 15,000$ case at 7 bar shows a stronger signal, and there does not appear to be a significant reduction in intensity from 3.5 to 7 bar for the higher Re_{jet} flames. This suggests that changes due to flow effects and flame stability have at least a partial impact on the chemiluminescence detected, although the much stronger signal at 1.1 and 2 bar hints at a fundamental change in behaviour at elevated pressures. The change in chemical kinetics behaviour with increasing pressure is examined in §3.5.

3.3. Statistical analysis of short-exposure images

The statistical behaviour of the flames can be examined in greater detail by analysing the short-exposure CH* images. A series of greater than 200 video frames for each case were included in the analysis, enabling the calculation of the mean and variation in the liftoff height. An adaptive thresholding algorithm was applied to each individual frame, which effectively isolates the flame base such that the liftoff height can be determined. This process, in-turn, enables the mean location of the liftoff height above the jet exit to be calculated, as well as the standard deviation. These results are plotted as a function of pressure in Fig. 5, with the standard deviation (σ_L) about the mean represented by the vertical bars; these values are also included in Table 2. The minimum and maximum liftoff heights (following removal of outliers) from the series of images are also displayed in Fig. 5 on the same set of axes.

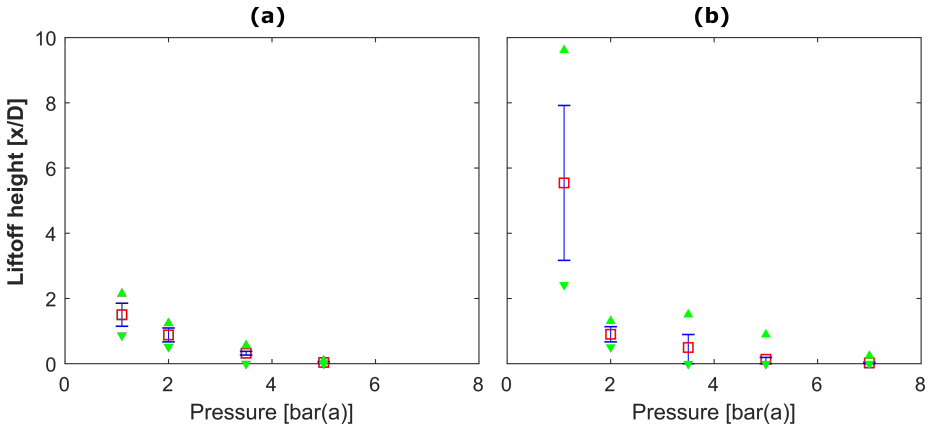

Figure 5: Mean liftoff height (indicated by red boxes) as a function of pressure for $Re_{jet} = 10,000$ (a) and $Re_{jet} = 15,000$ (b) flames, with vertical bars representing the standard deviation from the mean. Minimum and maximum liftoff heights from the series of images are also shown by the green markers, noting that the same axis limits are used for subfigures (a) and (b). Statistical values were calculated from a series of $>$ 200 CH* video frames for each case.

Table 2: Standard deviation values of liftoff height based on CH* video frames.

	σ_L $[x/D]$	
P [bar]	$Re_{jet} = 10$k	$Re_{jet} = 15$k
1.1	0.35	2.4
2.0	0.21	0.23
3.5	0.06	0.40
5.0	0.03	0.06
7.0	-	0.02

In the discussion surrounding the mean images shown in Fig. 4, the lack of a clearly defined flame base for the $Re = 15,000$, 1.1 bar case was noted.

The statistical results shown in Fig. 5 and Table 2 confirm the hypothesis that this is related to fluctuations in the liftoff height, with this case displaying not only an increased liftoff height, but significantly greater variation in this value in comparison to the other cases. This is also evident in the short-exposure (1–2.5 ms) OH^* images which may be found in Fig. S1 of the Supplementary Material. It has previously been observed that flames in the transition from the attached to the lifted regimes can show a sudden change in liftoff location with changes in the jet and coflow velocity [45], so it is possible that small fluctuations in the relative velocity are responsible for the variability of the flame base. It has also been observed previously that inhomogeneities in the temperature profile can have a significant effect on the liftoff height of JHC flames [46], which could also be responsible for this variability. Regardless of the mechanism, it can be seen that increasing the pressure from 1.1 to 2 bar has a significant effect for the $Re = 15,000$ flames, with the 2 bar case displaying a very similar liftoff behaviour to the corresponding $Re = 10,000$ flame. As the pressure is increased beyond 2 bar, the flames become stabilised at the jet exit, with a tendency for less fluctuation in the flame base; again, the instantaneous OH^* images shown in Fig. S1 support this. This change in stabilisation with pressure can be explained by the reduced velocity of the fuel stream at higher pressures, since velocity is inversely proportional to pressure for the flames with constant Re_{jet}.

3.4. Broadband flame imaging

To compare the broadband appearance of the flames at different pressures, true-colour images are shown in Fig. 6. These images correspond to jet flames with $Re_{jet} = 10,000$ and a coflow of 9% O_2 similar to Fig. 4, although with an increased coflow temperature of 1200 K. The typical flame photographs at $Re_{jet} = 15,000$ show very similar features and trends with pressure to those presented in Fig. 6 and are not included for brevity. All photographs were captured with an exposure time of 1/250 s in order to capture the turbulent sooting behaviour, and two photographs are shown for each operating pressure. Reduced ISO-speed settings on the camera were required to avoid saturation as the operating pressure was increased; these values are also displayed in the figure.

The true-colour images in Fig. 6 display a noticeable change in the sooting behaviour of the flames as the pressure is increased. For the 1.1 and 2.0 bar cases, a very faint blue/violet outline can be observed, while there is no evidence of soot formation. The lack of soot at 1.1 bar is consistent with observations for similar flames at atmospheric pressure, whereby soot formation is suppressed within the coflow-controlled region (which extends approximately 120 mm from the jet exit); this is true for flames of 1:1 NG:H_2 [23] as well as for unblended NG in a 9% O_2 coflow [47]. Notably, soot can be seen to form well within this region for the 5.0 and 7.0 bar cases shown in Fig. 6, which is a significant departure from the behaviour observed for low-pressure flames, particularly considering the fuel mixture being used. This is likely a result of a shift towards pyrolytic reactions

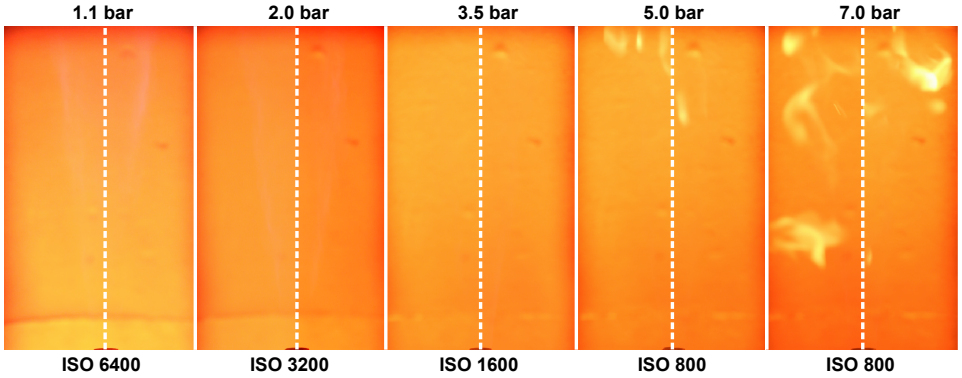

Figure 6: True-colour images of $Re_{jet} = 10,000$ CH_4/H_2 flames (1:1 blend) at 5 different operating pressures. All flames correspond to a 9% O_2 coflow and heat input of 15 kW.

at elevated pressure, which is examined further via laminar flame simulations in §3.5.

3.5. Laminar flame simulation results

To determine whether the changes in chemiluminescence intensity (§3.2) and sooting behaviour (§3.4) are a result of mixing/flow-field effects or purely chemical phenomena, laminar opposed-flow simulations were performed. Although the OH^* and CH^* sub-mechanisms that were used in the simulations are tailored for atmospheric-pressure combustion, they can be implemented in combination with the underlying kinetics mechanism, which is valid for elevated pressures. This facilitates comparisons against the experimental chemiluminescence results, to assess the suitability of the model in regard to predicting the underlying trends with increasing pressure. Fig. 7 displays the variation in the mass fraction of both OH^* and CH^* as a function of pressure, with strain rate held constant for the different pressures. Both the maximum and integrated values over the simulation domain are shown in Fig. 7, in order to account for the narrowing of the reaction zone as pressure is increased.

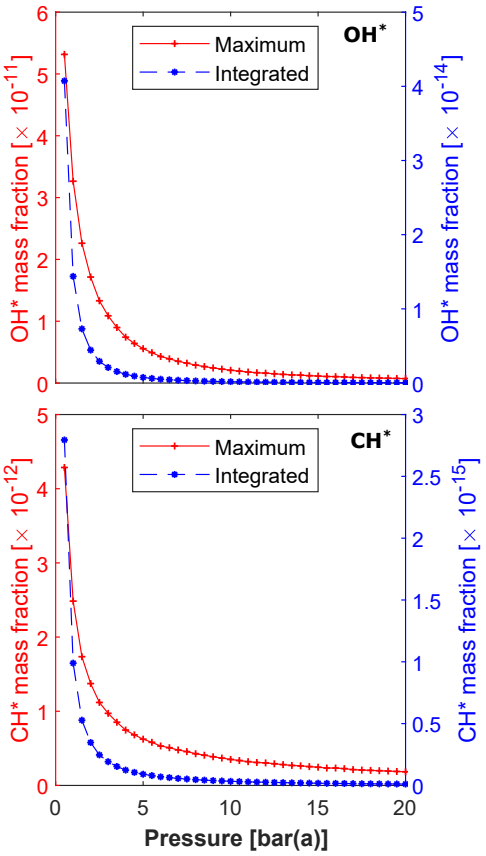

Figure 7: Variation in OH* (top) and CH* (bottom) for pressures ranging from 0.5 to 20 bar(a). Results are shown for the maximum mass fraction (in red) and integrated mass fraction (in blue) over the simulation domain.

Both OH* and CH* show a noticeable reduction with pressure based on the simulation results presented in Fig. 7. The reduction is particularly pronounced at lower pressures, in particular for the integrated OH* values up to $P \approx 3.0$ bar, at which point the mass fraction is reduced by a factor of 10 from the atmospheric-pressure value, after which further increases in pressure appear to be less significant. This generally supports the experimental observations, in which the most noticeable reduction in intensity was from 1.1–3.5 bar, although the 7 bar case was also seen to be of significantly lower intensity for the $Re = 10000$ case. The fact that there is a monotonic decrease in both the maximum and integrated values indicates that this reduction is not a direct consequence of a narrowing of the reaction zone, suggesting instead that it could be related to a change in the consumption and/or formation pathways as the pressure is increased. For OH*, this can be investigated by studying the rates of the two reactions which lead to OH* formation—that is, R1 and R2 (§2.3)—as a function of pressure, as shown in Fig. 8.

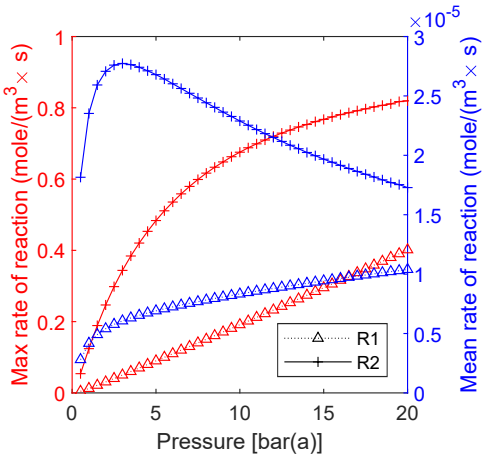

Figure 8: Variation in the formation rates of OH* for pressures ranging from 0.5 to 20 bar(a). Results are shown for the maximum rates (in red) and mean rates (in blue), with the contribution from R1 and R2 shown separately.

The plots shown in Fig. 8 show that reaction R2 is the main contributor to OH* formation at all pressures (in terms of both the maximum and mean formation rate), although R1 becomes more significant as the pressure is increased. Despite the clear reduction in the OH* mass fraction with pressure shown in Fig. 7, the maximum formation rate is seen to increase with pressure for both reactions; this is also the case for the mean rate of R1, while the mean rate of R2 shows a non-monotonic behaviour. These results indicate that, although the pressure does have an impact on the OH* formation pathways, this does not explain the reduced mass fractions observed in Fig. 7. It is important to note that, due to the short-lived nature of excited-state radicals such as OH* in a flame, the formation rate does not completely capture the overall behaviour in terms of the steady-state species concentrations. Therefore, it is important to understand the total or net rate of production (ROP), which in this analysis includes both formation and consumption (largely due to collisional quenching). The trends in net ROP as a function of pressure are shown in Fig. 10, along with the values of heat release rate (HRR) and OH* concentration ([OH*]), noting that the mass fraction and not the concentration was shown in Fig. 7. As mentioned in §2.3, the spontaneous emission process and associated relaxation to the ground state was included in the OH* sub-mechanism; this emission rate is also shown in Fig. 10. To facilitate comparison in terms of the trends with pressure, all of the values are normalised against their respective maxima across all pressures in Fig. 10. It should also be mentioned that the HRR values correspond to specific (i.e. density-normalised) heat release, to account for the increased mass flow as the pressure is increased.

The normalised values shown in Fig. 10 provide a number of interesting insights regarding the chemiluminescence behaviour. First of all, it is worth noting that the plots for the OH* decay rate and the OH* concentration are

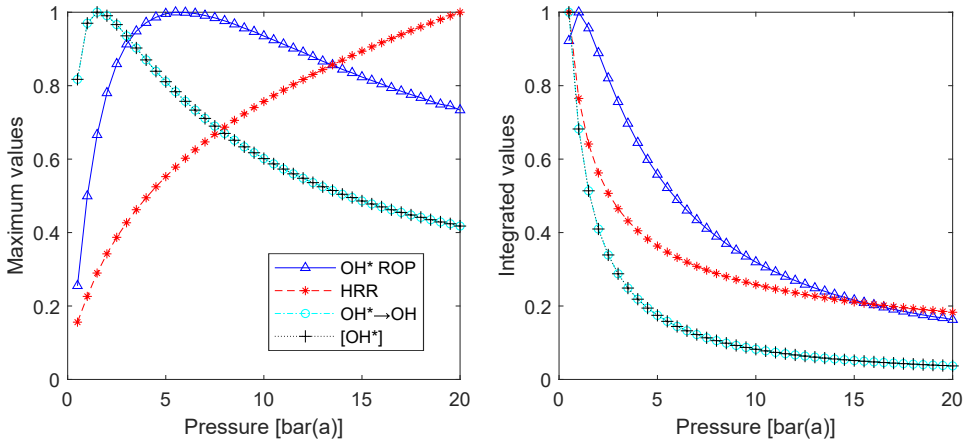

Figure 9: Normalised results displaying OH* concentration and spontaneous decay rate, as well as net ROP and heat release rate (HRR), for pressures ranging from 0.5 to 20 bar(a). Results are shown for the maximum values (left) and integrated values (right). Note that for ROP, the integrated values are calculated over the regions of positive net ROP only.

essentially coincident, both in terms of the maximum and integrated values; this is expected, since a constant rate coefficient was prescribed for reaction R5. The increase in the maximum OH* concentration at low pressures ($P \leq 1.5$) suggests that there are competing effects taking place in terms of the effect of pressure, noting that higher peak values of species concentrations are expected as the pressure is increased due to the narrowing of the reaction zone and the increase in density. This initial increase with pressure can also be seen for the maximum and integrated net ROP values, with the maximum ROP showing a significant increase up to approximately 7 bar and then decreasing slightly, while the integrated ROP only shows a slight increase from 0.5 - 1.0 bar. Interestingly, the maximum OH* concentration and the integrated ROP both show a similar trend with pressure. Since the formation rates show a general increase with pressure (at least for lower pressures in the case of R2) as shown in Fig. 8, it follows that the more rapid reduction in the net ROP—and the corresponding reduction in [OH*]—is related to the increased impact of collisional quenching at higher pressures. Indeed, the mixture-fraction-space profiles of formation and consumption—included in Figs. 2 and 3 of the Supplementary Material—show that an increase in formation is accompanied by an increase in consumption via quenching, which ultimately leads to a reduction in the net ROP at elevated pressures.

The normalised plots of specific heat release rate shown in Fig. 10 are also important to analyse, since chemiluminescence is commonly used as a practical method of indicating heat release. While the maximum HRR is seen to increase with pressure, the integrated values—which essentially represent the total heat release across the 1-D flame zone—show a reduction with pressure due to the narrowing of the reaction zone. It can also be seen that the integrated OH*

concentration shows a similar trend with pressure to HRR, although the former shows a more rapid reduction. These results highlight the importance of understanding the effects of pressure on chemiluminescence, particularly in terms of developing a quantitative relationship between chemiluminescence and HRR. It is also worth noting that it has previously been observed that changes in heat release rate with pressure are heavily dependent on flow characteristics, particularly when comparing the behaviour of laminar and turbulent flames [48]. Therefore, further efforts in developing the relationship between chemiluminescence and HRR should consider these effects, which can be achieved using both computational fluid dynamics (CFD) and more detailed experimental measurements via laser diagnostics, for example.

In the photographs shown in Fig. 6, it was observed that there is a significant increase in soot formation near the jet exit as the pressure is increased. Although the detailed chemistry relating to soot formation was not modelled in the simulations, it is possible to analyse the presence of regions of negative heat release; these regions are indicative of pyrolysis within the flame, which leads to the production of soot precursors [4]. Mixture-fraction-space profiles of net HRR are shown in Fig. 10, for five different pressures ranging from 1–7 bar(a). At 1 bar(a), two distinct positive peaks are observed in the heat release profile, which is typical of combustion with a high-temperature oxidant stream [4]. As the pressure is increased, this dual-peak behaviour is suppressed, with the cases at 5 and 7 bar(a) displaying a "shoulder" feature rather than a distinct secondary peak. The reaction-specific plots—which are included in the Supplementary Material for 1 and 7 bar(a)—show that this is due to an increase in the spatial overlap between the exothermic reactions as the pressure is increased, accompanied by a general narrowing of the positive heat release region. This is accompanied by an increased tendency for negative heat release as the pressure is increased, both in terms of net HRR and the reaction-specific profiles.

The results of these laminar flame simulations highlight the importance of understanding the effect of pressure on combustion under hot and low-O_2 conditions. The narrowing of the reaction zone and reduced chemical time-scales which occur with increasing pressure appears to promote a transition away from features typically associated with the mild combustion regime, such as a broadening of the OH profile and an absence of negative heat release regions [4]. The chemiluminescence behaviour is shown to be particularly sensitive to pressure, with both the OH^* and CH^* maximum and integrated mass fractions displaying a monotonic reduction with pressure. Further analysis of the OH^* formation reactions and net ROP rates suggests that there are competing effects present leading to non-monotonic trends, particularly at lower pressures. Furthermore, the analysis indicates that the general reduction in OH^* with pressure is due to a combination of a shift in the formation pathways and an increased impact of collisional quenching at elevated pressures. These findings are particularly important for informing future research directions, which will involve extending the 1-D simulations to a more realistic CFD model with geometry and flow conditions matching those of the CP-JHC.

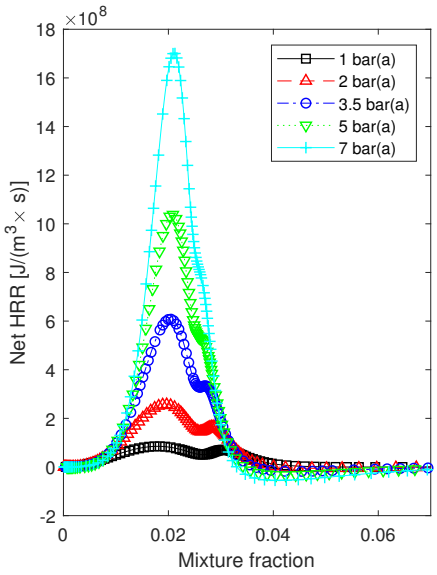

Figure 10: Profiles of net HRR as a function of mixture fraction, for pressures ranging from 1–7 bar(a).

4. Conclusions

The characteristics of confined-and-pressurised, turbulent jet flames have been investigated, using a novel burner configuration which facilitates the control of coflow conditions. The CP-JHC enables the parametric analysis of the effects of coflow temperature and oxygen concentration, as well as turbulent and chemical timescales and how these change with elevated pressure. A detailed description of the key features and capabilities of the apparatus has been provided in this paper. Temperature measurements of the coflow stream indicate an increase in enthalpy deficit as the pressure is increased, due to increased heat losses to the combustor walls. Turbulent jet flames of NG/H_2 were examined in terms of both targeted chemiluminescence and broadband imaging. Changes in flame stability were observed for variations in both Reynolds number and pressure, with an increased tendency for flame attachment at elevated pressures, as well as a reduction in OH^* and CH^* and an increase in soot formation.

The effect of pressure on the chemiluminescence behaviour and heat release rate was examined numerically via laminar flame simulations, which highlighted a fundamental change in behaviour at elevated pressures. In particular, both the OH^* and CH^* mass fractions were observed to show a reduction with pressure in line with the experimental observations, suggesting that the atmospheric-pressure chemiluminescence sub-mechanisms can provide at least a qualitative indication of the trends with increasing pressure. Further analysis in regards to the OH^* behaviour indicates that this reduction is related to an increase in

collisional quenching, which counteracts the increase in the rate of formation at lower pressures. Additionally, a narrowing of the reaction zone and a more prominent negative heat release region is observed with pressure, highlighting the challenges associated with the adoption of mild combustion in practical configurations such as gas turbines. This in-turn emphasises the need for further investigation into the fundamental combustion behaviour under such conditions, which the CP-JHC apparatus will facilitate.

References

[1] A. Perpignan, A. Gangoli Rao, D. Roekaerts, Flameless combustion and its potential towards gas turbines, Progress in Energy and Combustion Science 69 (2018) 28–62.

[2] J. A. Wünning, J. G. Wünning, Flameless oxidation to reduce thermal no-formation, Progress in Energy and Combustion Science 23 (1) (1997) 81–94.

[3] A. Cavaliere, M. de Joannon, Mild Combustion, Progress in Energy and Combustion Science 30 (4) (2004) 329–366.

[4] M. de Joannon, P. Sabia, G. Cozzolino, G. Sorrentino, A. Cavaliere, Pyrolitic and Oxidative Structures in Hot Oxidant Diluted Oxidant (HODO) MILD Combustion, Combustion Science and Technology 184 (7-8) (2012) 1207–1218. doi:10.1080/00102202.2012.664012.

[5] F. Joos, P. Brunner, B. Schulte-Werning, K. Syed, A. Eroglu, Development of the Sequential Combustion System for the ABB GT24/GT26 Gas Turbine Family, in: Volume 4: Heat Transfer; Electric Power; Industrial and Cogeneration, AMSE, Birmingham, UK, 1996.

[6] D. Ballal, J. Zelina, Progress in Aeroengine Technology (1939–2003), Journal of Aircraft 41 (1) (2004) 43–50.

[7] F. Güthe, J. Hellat, P. Flohr, The Reheat Concept: The Proven Pathway to Ultralow Emissions and High Efficiency and Flexibility, Journal of Engineering for Gas Turbines and Power 131 (2) (Mar. 2009).

[8] Y. Levy, V. Erenburg, V. Sherbaum, I. Gaissinski, Flameless Oxidation Combustor Development for a Sequential Combustion Hybrid Turbofan Engine, in: ASME Turbo Expo 2016: Turbomachinery Technical Conference and Exposition, AMSE Digital Collection, 2016.

[9] A. a. V. Perpignan, A. G. Rao, Effects of chemical reaction mechanism and NOx formation pathways on an inter-turbine burner, The Aeronautical Journal 123 (1270) (2019) 1898–1918.

[10] J. Ye, P. Medwell, E. Varea, S. Kruse, B. Dally, H. Pitsch, An experimental study on MILD combustion of prevaporised liquid fuels, Applied Energy 151 (2015) 93–101.

[11] V. Nori, J. Seitzman, Evaluation of Chemiluminescence as a Combustion Diagnostic Under Varying Operating Conditions, in: 46th AIAA Aerospace Sciences Meeting and Exhibit, American Institute of Aeronautics and Astronautics. doi:10.2514/6.2008-953.

[12] B. Higgins, M. Q. McQuay, F. Lacas, J. C. Rolon, N. Darabiha, S. Candel, Systematic measurements of OH chemiluminescence for fuel-lean, high-pressure, premixed, laminar flames, Fuel 80 (1) (2001) 67–74. doi:10.1016/S0016-2361(00)00069-7.

[13] S. Sardeshmukh, M. Bedard, W. Anderson, The use of OH* and CH* as heat release markers in combustion dynamics, International Journal of Spray and Combustion Dynamics 9 (4) (2017) 409–423. doi:10.1177/1756827717718483.

[14] W. Boyette, A. Elbaz, T. Guiberti, W. Roberts, Experimental investigation of the near field in sooting turbulent nonpremixed flames at elevated pressures, Experimental Thermal and Fluid Science 105 (2019) 332–341. doi:10.1016/j.expthermflusci.2019.04.008.

[15] K. Young, C. Stewart, J. Moss, Soot formation in turbulent nonpremixed kerosine-air flames burning at elevated pressure: Experimental measurement, Symposium (International) on Combustion 25 (1) (1994) 609–617. doi:10.1016/S0082-0784(06)80692-2.

[16] W. Boyette, T. Guiberti, G. Magnotti, W. Roberts, Structure of turbulent nonpremixed syngas flames at high pressure, Proceedings of the Combustion Institute 37 (2) (2019) 2207–2214. doi:10.1016/j.proci.2018.09.004.

[17] R. Lückerath, W. Meier, M. Aigner, FLOX{$\hat{\{}$®}$} Combustion at High Pressure With Different Fuel Compositions, Journal of Engineering for Gas Turbines and Power 130 (1) (2008) 011505.

[18] H. Schütz, R. Lückerath, T. Kretschmer, B. Noll, M. Aigner, Analysis of the Pollutant Formation in the FLOX® Combustion, Journal of Engineering for Gas Turbines and Power 130 (1) (Jan. 2008). doi:10.1115/1.2747266.

[19] J. M. Fleck, P. Griebel, A. M. Steinberg, C. M. Arndt, M. Aigner, Autoignition and flame stabilization of hydrogen/natural gas/nitrogen jets in a vitiated cross-flow at elevated pressure, International Journal of Hydrogen Energy 38 (36) (2013) 16441–16452. doi:10.1016/j.ijhydene.2013.09.137.

[20] O. Schulz, N. Noiray, Combustion regimes in sequential combustors: Flame propagation and autoignition at elevated temperature and pressure, Combustion and Flame 205 (2019) 253–268. doi:10.1016/j.combustflame.2019.03.014.

[21] F. Guethe, D. Guyot, G. Singla, N. Noiray, B. Schuermans, Chemiluminescence as diagnostic tool in the development of gas turbines, Applied Physics B 107 (3) (2012) 619–636. doi:10.1007/s00340-012-4984-y.

[22] B. Dally, A. Karpetis, R. Barlow, Structure of turbulent non-premixed jet flames in a diluted hot coflow, Proceedings of the Combustion Institute 29 (1) (2002) 1147–1154.

[23] P. Medwell, P. Kalt, B. Dally, Simultaneous Imaging of OH, Formaldehyde, and Temperature of Turbulent Nonpremixed Jet Flames in a Heated and Diluted Coflow, Combustion and Flame 148 (1-2) (2007) 48–61.

[24] R. Cabra, T. Myhrvold, J. Chen, R. Dibble, A. Karpetis, R. Barlow, Simultaneous laser raman-rayleigh-lif measurements and numerical modeling results of a lifted turbulent H2/N2 jet flame in a vitiated coflow, Proceedings of the Combustion Institute 29 (2) (2002) 1881–1888.

[25] R. Gordon, A. Masri, E. Mastorakos, Simultaneous Rayleigh temperature, OH- and CH2O-LIF imaging of methane jets in a vitiated coflow, Combustion and Flame 155 (1) (2008) 181–195.

[26] G. P. Smith, D. M. Golden, M. Frenklach, N. W. Moriarty, B. Eiteneer, M. Goldenberg, C. T. Bowman, R. K. Hanson, S. Song, W. C. G. Jr., V. V. Lissianski, Z. Qin, GRI-Mech 3.0, http://combustion.berkeley.edu/gri-mech/version30/text30.html#cite (2000).

[27] F. C. Christo, B. B. Dally, Modeling turbulent reacting jets issuing into a hot and diluted coflow, Combustion and Flame 142 (1) (2005) 117–129. doi:10.1016/j.combustflame.2005.03.002.

[28] M. J. Evans, P. R. Medwell, Z. F. Tian, Modeling Lifted Jet Flames in a Heated Coflow Using an Optimized Eddy Dissipation Concept Model, Combustion Science and Technology 187 (7) (2015) 1093–1109.

[29] S. R. Shabanian, P. R. Medwell, M. Rahimi, A. Frassoldati, A. Cuoci, Kinetic and fluid dynamic modeling of ethylene jet flames in diluted and heated oxidant stream combustion conditions, Applied Thermal Engineering 52 (2) (2013) 538–554. doi:10.1016/j.applthermaleng.2012.12.024.

[30] J. A. M. Sidey, E. Mastorakos, Simulations of laminar non-premixed flames of methane with hot combustion products as oxidiser, Combustion and Flame 163 (2016) 1–11. doi:10.1016/j.combustflame.2015.07.034.

[31] M. Ihme, Y. C. See, LES flamelet modeling of a three-stream MILD combustor: Analysis of flame sensitivity to scalar inflow conditions, Proceedings of the Combustion Institute 33 (1) (2011) 1309–1317. doi:10.1016/j.proci.2010.05.019.

[32] M. Ihme, Y. C. See, Prediction of autoignition in a lifted methane/air flame using an unsteady flamelet/progress variable model, Combustion and Flame 157 (10) (2010) 1850–1862. doi:10.1016/j.combustflame.2010.07.015.

[33] R. N. Roy, S. Kumar, S. Sreedhara, A new approach to model turbulent lifted CH4/air flame issuing in a vitiated coflow using conditional moment closure coupled with an extinction model, Combustion and Flame 161 (1) (2014) 197–209. doi:10.1016/j.combustflame.2013.08.007.

[34] A. Kazakov, M. Frenklach, Reduced Reaction Sets based on GRI-Mech 1.2, http://combustion.berkeley.edu/drm/.

[35] A. Parente, M. R. Malik, F. Contino, A. Cuoci, B. B. Dally, Extension of the Eddy Dissipation Concept for turbulence/chemistry interactions to MILD combustion, Fuel 163 (2016) 98–111. doi:10.1016/j.fuel.2015.09.020.

[36] M. T. Lewandowski, Z. Li, A. Parente, J. Pozorski, Generalised Eddy Dissipation Concept for MILD combustion regime at low local Reynolds and Damköhler numbers. Part 2: Validation of the model, Fuel 278 (2020) 117773. doi:10.1016/j.fuel.2020.117773.

[37] N. Romero-Anton, X. Huang, H. Bao, K. Martin-Eskudero, E. Salazar-Herran, D. Roekaerts, New extended eddy dissipation concept model for flameless combustion in furnaces, Combustion and Flame 220 (2020) 49–62. doi:10.1016/j.combustflame.2020.06.025.

[38] A. De, E. Oldenhof, P. Sathiah, D. Roekaerts, Numerical Simulation of Delft-Jet-in-Hot-Coflow (DJHC) Flames Using the Eddy Dissipation Concept Model for Turbulence–Chemistry Interaction, Flow, Turbulence and Combustion 87 (4) (2011) 537–567. doi:10.1007/s10494-011-9337-0.

[39] C. Galletti, A. Parente, M. Derudi, R. Rota, L. Tognotti, Numerical and experimental analysis of NO emissions from a lab-scale burner fed with hydrogen-enriched fuels and operating in MILD combustion, International Journal of Hydrogen Energy 34 (19) (2009) 8339–8351. doi:10.1016/j.ijhydene.2009.07.095.

[40] J. M. Hall, E. L. Petersen, An optimized kinetics model for OH chemiluminescence at high temperatures and atmospheric pressures, International Journal of Chemical Kinetics 38 (12) (2006) 714–724. doi:10.1002/kin.20196.

[41] R. M. I. Elsamra, S. Vranckx, S. A. Carl, CH(A2Δ) Formation in Hydrocarbon Combustion: The Temperature Dependence of the Rate Constant of the Reaction C2H + O2 –> CH(A2Δ) + CO2, The Journal of Physical Chemistry A 109 (45) (2005) 10287–10293. doi:10.1021/jp053684b.

[42] M. Tamura, P. A. Berg, J. E. Harrington, J. Luque, J. B. Jeffries, G. P. Smith, D. R. Crosley, Collisional Quenching of CH(A), OH(A), and NO(A) in Low Pressure Hydrocarbon Flames, Combustion and Flame 114 (3) (1998) 502–514. doi:10.1016/S0010-2180(97)00324-6.

[43] W. L. Dimpfl, J. L. Kinsey, Radiative lifetimes of OH(A2Σ) and Einstein coefficients for the A-X system of OH and OD, Journal of Quantitative Spectroscopy and Radiative Transfer 21 (3) (1979) 233–241. doi:10.1016/0022-4073(79)90014-1.

[44] Y. Liu, J. Tan, H. Wang, L. Lv, Characterization of heat release rate by OH* and CH* chemiluminescence, Acta Astronautica 154 (2019) 44–51. doi:10.1016/j.actaastro.2018.10.022.

[45] S. D. Terry, K. M. Lyons, Turbulent Lifted Flames in the Hysteresis Regime and the Effects of Coflow, Journal of Energy Resources Technology 128 (4) (2006) 319–324. doi:10.1115/1.2358147.

[46] E. Oldenhof, M. J. Tummers, E. H. van Veen, D. J. E. M. Roekaerts, Role of entrainment in the stabilisation of jet-in-hot-coflow flames, Combustion and Flame 158 (8) (2011) 1553–1563. doi:10.1016/j.combustflame.2010.12.018.

[47] M. Evans, A. Chinnici, P. Medwell, J. Ye, Ignition features of methane and ethylene fuel-blends in hot and diluted coflows, Fuel 203 (2017) 279–289.

[48] X. Wang, T. Jin, Y. Xie, K. H. Luo, Pressure effects on flame structures and chemical pathways for lean premixed turbulent H2/air flames: Three-dimensional DNS studies, Fuel 215 (2018) 320–329. doi:10.1016/j.fuel.2017.10.094.